Relationships between crystal morphology and composition in the (Ba,Sr)SO_4–H_2O solid solution–aqueous solution system

N. Sánchez-Pastor *, C.M. Pina, L. Fernández-Díaz

Departamento de Cristalografía y Mineralogía, Universidad Complutense de Madrid, 28040, Madrid, Spain

Abstract

This paper deals with the relationship between habit and compositional changes in crystals of the $Ba_xSr_{1-x}SO_4$ solid solution at 25 °C and 1 atm. Crystals corresponding to the whole range of compositions of the $Ba_xSr_{1-x}SO_4$ solid solution have been grown in a diffusing–reacting system. The physicochemical evolution resulting from counter-diffusion of $SrCl_2$/$BaCl_2$ and Na_2SO_4 reactants along a silica hydrogel column results in the development of spatio-temporal crystallization sequences. The external habit and the internal zoning reflecting both the morphological and compositional evolution of the crystals have been studied by scanning electron microscopy, EDAX and microprobe analysis. As composition varies from barite to celestite end-members, a clear evolution both in internal crystal morphologies and in final habit of crystals grown along the gel column has been observed. The main change observed is in the relative development of {001} and {011} forms, which is accompanied by a change in the crystals elongation. While tabular habits dominated by the {001} pinacoid correspond to crystal compositions close to pure barite, crystals with compositions closer to celestite show elongated morphologies dominated by the {011} rhombic prism. This variation is also evident in the internal morphologies of the crystals. The progressive predominance of {011} forms as crystals become richer in Sr has been interpreted on the basis of surface structure description by Hartman–Perdok theory. Moreover, Atomic Force Microscopy investigations of the epitaxial growth of pure celestite on barite (001) surfaces under different degrees of supersaturation with respect to celestite have provided complementary quantitative information. Growth morphologies for different supersaturations with respect to celestite can be predicted using growth rates of crystal faces measured on a molecular scale. The results clearly show the effect of Sr incorporation into barite structure on the $Ba_xSr_{1-x}SO_4$ crystal habit at a molecular scale. The results presented in this paper can help to develop morphological criteria relating morphology and composition of $Ba_xSr_{1-x}SO_4$ crystals occurring in natural environments as a result of inorganic crystallization and biomineralization processes.

Keywords: Barite; Celestite; Crystal morphology; Gel crystal growth method; AFM; Crystal growth rates

1. Introduction

The barite–celestite solid solution, $Ba_xSr_{1-x}SO_4$, occurs in a wide variety of rock formations from Archean to present times. Barites and celestites, as well as intermediate composition members of the solid solution, can form from seawater as authigenic minerals or as a result of hydrothermal and diagenetic processes (Feely, 1987). The origin of authigenic $Ba_xSr_{1-x}SO_4$ is controversial given that most oceanic waters are undersaturated in barite (Rushdi et al., 2000). Several authors have proposed that marine barite forms by inorganic precipitation from seawater in sulphate-enriched micro-

* Corresponding author.
E-mail addresses: nsanchez@geo.ucm.es (N. Sánchez-Pastor), cmpina@geo.ucm.es (C.M. Pina), lfdiaz@geo.ucm.es (L. Fernández-Díaz).

environments where the origin of sulphate would be mainly related to organic matter oxidation (Bishop, 1988; Chow and Goldberg, 1960). A biogenic origin has also been proposed for marine barite, although very few planktonic organisms directly precipitate this mineral. On the other hand, diagenetic barite formation has been related by several authors to the creation of Ba-rich microenvironments, where either the dissolution of achantarian skeletons (Bernstein et al., 1992; Bernstein and Byrne, 2004) or the decay of phytoplankton (Ganeshram et al., 2003) are a source of barium. Authigenic barite–celestite crystals can be used to monitor seawater strontium and sulphur isotopic composition which in turn provide clues to climate changes, atmospheric chemistry, ocean productivity, etc. (Kastner, 1999; Paytan et al., 1993; Claypool et al., 1980). Therefore, a detailed study of natural barite–celestite solid solutions may be extremely useful to characterize present and ancient biogeological environments.

One of the prerequisites for using properly $Ba_xSr_{1-x}SO_4$ natural solid solutions as proxies of geological conditions is to distinguish between marine and hydrothermal crystals. Frequently, criteria based on crystal morphology are invoked to make such a distinction (Dehairs et al., 1980; Bishop, 1988; Paytan et al., 2002). As Paytan et al. (2002) have pointed out, authigenic barite crystals are smaller than 5 μm and ellipsoidal in shape, while diagenetic and hydrothermal barite crystals range in size from 20 to 70 μm. Diagenetic barite crystals are flat, tabular shaped, while hydrothermal barites occur in rosettes formed by intergrown tabular individuals.

Crystals of $Ba_xSr_{1-x}SO_4$ can be easily grown using the silica hydrogel technique. Previous work has provided extensive information on the nucleation and growth conditions of barite, celestite, and intermediates members of the $Ba_xSr_{1-x}SO_4$ solid solution (Prieto et al., 1990, 1993, 1997). The main advantage of silica hydrogel technique is that the gel limits convection and advection, so that mass-transfer only occurs by diffusion. As a consequence, the number of nuclei that form is reduced. Nucleation takes place under known conditions of supersaturation and supersaturation rate, i.e. the rate at which the system departs from equilibrium (Prieto et al., 1990, 1991, 1994). Nucleation of both barite and celestite in gels requires high supersaturation. However, the supersaturation threshold value is around two orders of magnitude higher for barite than for celestite (Putnis et al., 1992; Prieto et al., 1993, 1997), in agreement with the much lower solubility of the former (log K_{sp} are -9.96 for $BaSO_4$ and -6.62 for $SrSO_4$; (Blount, 1977; Reardon and Armstrong, 1987).

In this paper we present an experimental study on the morphological changes of $Ba_xSr_{1-x}SO_4$ crystals as a function of their chemical composition. Crystals were grown from aqueous solutions in a diffusion–reaction system. By varying the barium molar fraction, $X_{[Ba^{2+}],aq}=[Ba^{2+}]/([Ba^{2+}]+[Sr^{2+}])$, of the starting solutions from 0 to 1, $Ba_xSr_{1-x}SO_4$ crystals with a wide compositional range were obtained and their morphology documented. Atomic Force Microscopy (AFM) observations of pure $SrSO_4$ growing on barite (001) faces showed nanotopographic changes. Growth rates were measured, providing information on the relationship between composition and morphology of the crystals.

2. Experimental procedure

2.1. Gel experiments and characterization methods

The silica gel technique has been extensively used as a method of growing crystals of sparingly soluble salts (carbonates, sulphates, etc.) from aqueous solutions (Henisch, 1988). The silica hydrogel is a porous medium with a sheet-like structure that forms interconnecting cells. Reactants are brought together by diffusion through the gel and, subsequently, nucleation and crystal growth occur by chemical reaction.

The experimental set up used in this work consists in a counter-diffusion system in which reservoirs A and B of two reagents are separated by a column of polymerized silica gel. The gel column was 280 mm long and 9 mm in diameter (Fig. 1). In order to localize nucleation events, gel column is considered to be divided into 28 slices of 1 cm width each, counted from reservoir A. The gel was prepared by acidification of a sodium silicate (Na_2SiO_3) solution to desired pH (5.5) by adding HCl (1N). After it polymerized to a solid gel, reservoirs A and B were filled with 8 cm^3 of $BaCl_2+SrCl_2$ and

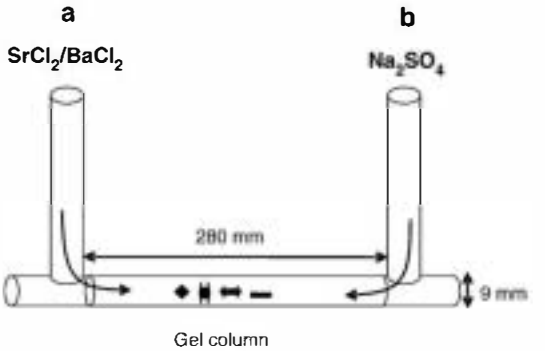

Fig. 1. Schematic representation of the experimental system.

Table 1
Composition and barium molar fraction of mother solutions used in the gel experiments

Experiment number	Mother solution A		$X_{[Ba^{2+}],aq} = \frac{[Ba^{2+}]}{[Ba^{2+}] + [Sr^{2+}]}$	Mother solution B
	$BaCl_2$ (mol/l)	$SrCl_2$ (mol/l)		Na_2SO_4 (mol/l)
1	0.1	0.9	0.1	0.25
2	0.2	0.8	0.2	0.25
3	0.3	0.7	0.3	0.25
4	0.4	0.6	0.4	0.25
5	0.5	0.5	0.5	0.25
6	0.6	0.4	0.6	0.25
7	0.7	0.3	0.7	0.25
8	0.8	0.2	0.8	0.25
9	0.9	0.1	0.9	0.25

Na_2SO_4 solutions, respectively. The initial concentrations of the solutions used are listed in Table 1. As can be seen, the initial molar fraction of Ba^{2+} in reservoir A was varied from 0.1 to 0.9, while Na_2SO_4 initial concentration in reservoir B was 0.25 mol/l in all the experiments. The reagents counter-diffuse through the silica gel column and, when they eventually meet, $Ba_xSr_{1-x}SO_4$ crystals precipitate as a reaction product. All the experiments were carried out at 25 °C.

Nucleation behaviour was characterized by monitoring the site of the first precipitate, and the time required for the first crystallites to become visible under a magnification of ×500. Changes in the crystals were monitored by optical microscopy. Two months after nucleation, the crystals were recovered by dissolving the gel in a NaOH (1 M) solution. Crystals displaying a representative range of morphologies obtained were hand-picked and studied by scanning electron microscopy (JEOL JSM6400, 40 kV, fitted with a LINK Ex1 energy dispersive spectrometer). Their mineralogy was confirmed by X-ray powder diffraction using a Siemens D500 unit.

In order to study possible compositional zonation patterns, the crystals were cut, polished, carbon coated and studied by back scattered electron (BSE) imaging. Variations in composition lead to variations in image brightness (Lloyd, 1987) which allows barium-rich regions and strontium-rich regions to be distinguished. Quantitative and semi-quantitative analysis of the crystals were obtained by electron microprobe (JEOL Superprobe JXA-8900 M) and EDAX, respectively.

2.2. AFM experiments

AFM experiments shown in this paper were conducted at 25 °C using a Digital Instruments Multimode AFM equipped with a fluid cell. Natural barite crystals freshly cleaved on (001) faces were used as substrates. Immediately after cleavage, samples were placed in the fluid cell of the AFM and aqueous solutions supersaturated with respect to celestite were passed over the substrates. The composition of the aqueous solutions is listed in Table 2. The activity coefficients of the different chemical species were calculated using the code PHREEQC (Parkhurst and Appelo, 2000). Supersaturation was calculated using the following expression:

$$\beta_{celestite} = \frac{a(Sr^{2+})a(SO_4^{2-})}{K_{sp}} \quad (1)$$

where $a(Sr^{2+})$ and $a(SO_4^{2-})$ are the activities of the Sr^{2+} and SO_4^{2-} ions in the solution and $K_{sp}=10^{-6.63}$ is the solubility product for celestite. Solutions with increas-

Table 2
Concentrations, calculated ionic activities for Ba^{2+} and SO_4^{2-} species and supersaturations with respect to celestite of the solutions used in the AFM experiments

Experiment number	Solution composition				Supersaturation
	$SrCl_2$ (mmol/l)	Na_2SO_4 (mmol/l)	$a(Sr^{2+})$	$a(SO_4^{2-})$	$\beta_{celestite}$
1	1.4	1.4	8.7×10^{-4}	8.6×10^{-4}	3.24
2	2.6	2.6	1.4×10^{-3}	1.3×10^{-3}	8.32
3	4	4	1.9×10^{-3}	1.8×10^{-3}	15.49
4	5.5	5.5	2.4×10^{-3}	2.3×10^{-3}	23.99
5	6	6	2.5×10^{-3}	2.4×10^{-3}	26.91
6	7	7	2.8×10^{-3}	2.6×10^{-3}	33.11
7	8	8	3.1×10^{-3}	2.9×10^{-3}	39.81

Table 3
Initial concentrations and experimental data for nucleation in the gel experiments

Experiment number	Mother solutions Ba/Sr/SO_4 (mol/l)	First nucleation position*	Waiting time 1st nucleation (h)	Second nucleation position*	Waiting time 2nd nucleation (h)	Third nucleation position*	Waiting time 3rd nucleation (h)
1	0.1/0.9/0.25	14	432	15	432	16	480
2	0.2/0.8/0.25	14–15	432	16	480	17	504
3	0.3/0.7/0.25	14–15	432	16	480	17	504
4	0.4/0.6/0.25	15	432	16–17	600	18	624
5	0.5/0.5/0.25	15	432	16–17	648	18	672
6	0.6/0.4/0.25	15	432	16–17	696	18	744
7	0.7/0.3/0.25	15	432	16–17	720	18	792
8	0.8/0.2/0.25	15–16	432	17–18	720	–	–
9	0.9/0.1/0.25	15–16	432	–	–	–	–

* Distance in cm from reservoir A (see Fig. 1).

ing supersaturation with respect to celestite were used in separate experiments. To maintain supersaturation, fresh solution was injected at intervals of about 1 min between each AFM scan. Growth rates for the crystal barite (100), (210), (001) and (011) planes were determined from sequences of AFM images. In the case of (100) and (210) planes, growth rates were measured along perpendicular directions to these planes on AFM deflection images of barite (001) surfaces; growth rates for (001) plane were measured from AFM height images. Finally, growth rates for (011) planes were obtained by combining height measurements on the (001) surface (along the [010] direction) using simple vector calculus.

3. Results

3.1. Morphological and compositional evolution of the $Ba_xSr_{1-x}SO_4$ crystals

The crystallization sequences observed in the gel experiments show a number of common features (see Table 3). The first nucleation event was always detected after 432 h of starting counter-diffusion. The location of the first crystallites depends on the $X_{[Ba^{2+}],aq}$ in reservoir A. Thus, when $X_{[Ba^{2+}],aq}$ is 0.1, the first crystals form in slice 14. The position of the first nucleation event moves towards reservoir B with increasing $X_{[Ba^{2+}],aq}$, to reach slice 16 when $X_{[Ba^{2+}],aq}$ is 0.9. These crystals show a tabular habit defined by {001} and {210} as the main forms and {100} as a relatively frequent minor form (Fig. 2a). Crystal size ranges from 80 to 180 μm. In the following days, new crystals nucleate in adjacent slices (15 to 18) toward the Na_2SO_4 reservoir. These crystals show a decrease in relative importance of the {001} pinacoid and a progressive development of rough surfaces corresponding approximately to a {0 1 1} rhombic prism. The development of rough {0 1 1} surfaces increases with the distance from the initial nucleation region, leading to the formation of crystals with a characteristic "arrow-like" habit closer to the Na_2SO_4 reservoir (Fig. 2b,c). Finally a third nucleation event in slices 16 to 18 (depending on the initial mother solutions) leads to the formation of very elongated "needle-like" crystals with a habit dominated by {0 1 1} and minor {210} faces (Fig. 2d). Fig. 2 shows a typical and complete morphological sequence. For some solution compositions specific habits either are not observed or are restricted to a very narrow region of the gel column. Thus, for very Sr-rich solutions (experiments 1 and 2, solutions with $X_{[Ba^{2+}],aq}$=0.1 and 0.2, respectively) tabular crystals are scarce and arrow-like habits predominate. Conversely, no needle-like crystals (experiment 8, solution with $X_{[Ba^{2+}],aq}$=0.8) and neither arrow-type nor needle-like crystals (experiment 9, solution with $X_{[Ba^{2+}],aq}$=0.9) formed from Ba-rich solutions.

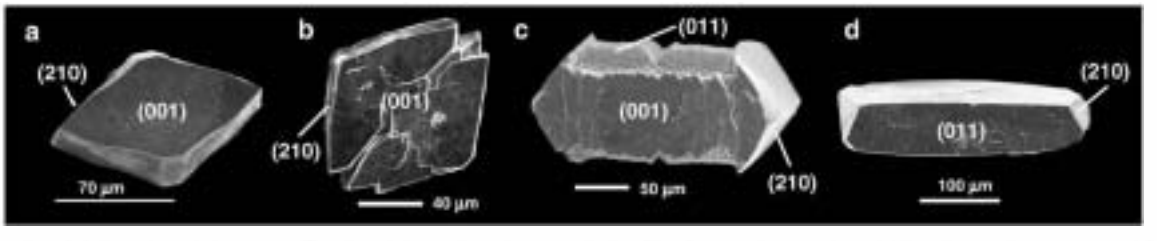

Fig. 2. Typical morphological sequence observed in the gel experiments. Example of (a) tabular crystals, (b) short arrow-like crystals, (c) long arrow-like crystals, (d) needle-like crystals.

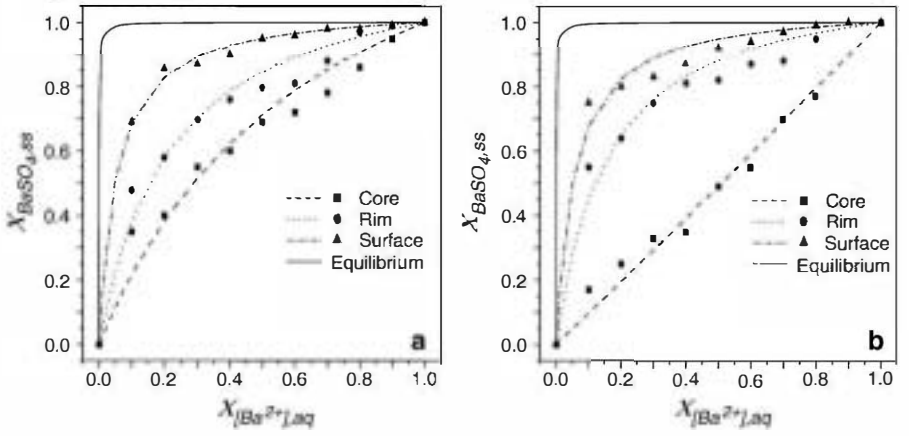

Fig. 3. Roozeboom diagrams constructed using compositional microprobe analysis of polished sections and EDAX analysis of crystal surfaces, corresponding to (a) tabular crystals, (b) arrow-like crystals. Solid lines correspond to the equilibrium Roozeboom line for this system.

The morphological sequence described above shows a relationship to the composition of the crystals. While tabular crystals are Ba-rich, needle-like habits correspond to crystals with much higher Sr contents. Thus, a connection between Sr-content and the relative elongation of the crystals along [100] is observed.

The actual $X_{BaSO_4,ss}$ in the crystal strongly depends on the initial $X_{[Ba^{2+}],aq}$ in reservoir A. Crystals grown

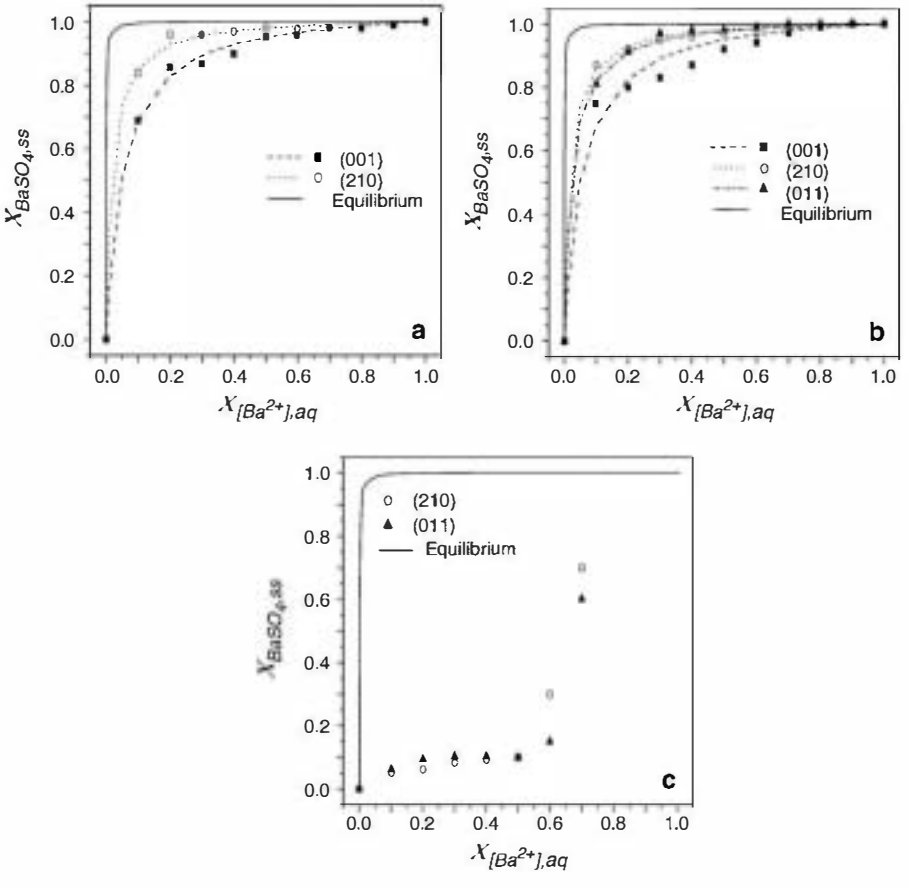

Fig. 4. Roozeboom diagrams constructed using compositional EDAX analysis of the different surfaces, carried out on crystals corresponding to different morphological groups and which had been obtained after diffusion periods of 1680 h: (a) tabular crystal, (b) arrow-like crystal and (c) needle-like crystal.

from Ba-rich mother solutions have higher $X_{BaSO_4,ss}$ than those grown from Sr-rich mother solutions. Moreover, the incorporation of Sr and Ba into the crystals is not homogeneous, but changes from core to surface. In all experiments crystals formed in both the first and the second nucleation regions show a Sr-rich core. This core-to-rim decrease in the Sr content is sharp in crystals of the second nucleation region and less evident in crystals of the first nucleation region. Finally, crystals formed in the third region are virtually pure celestite with a very small Ba-rich core. The variation of the $X_{BaSO_4,ss}$ of the crystal from core-to-rim with respect to the parent solution composition can be easily visualized by using Roozeboom diagrams. In such diagrams, $X_{BaSO_4,ss}$ the molar fraction of $BaSO_4$ in the $Ba_xSr_{1-x}SO_4$ solid solution, is plotted against $X_{[Ba^{2+}],aq}$, the molar fraction of Ba^{2+} in the mother solution. Roozeboom diagrams (Fig. 3) were constructed from compositional microprobe analysis of polished sections and EDAX analysis of surfaces of tabular and arrow-like crystals representative of the whole series of experiments. It is important to note here that only those values corresponding to the core of crystals from the first nucleation region can be considered as representative of the distribution coefficient between the growing crystal and the surrounding solution. The core-to-rim trends describe the compositional evolution of the system in response to changes in the initial mother solutions. The progressive enrichment of the crystal in Ba from core-to-rim is expressed in the increasing curvature of Roozeboom lines as crystal growth proceeds.

On the other hand, EDAX analyses show that each crystallographic form has its own distribution coefficient. Since all the crystals were removed from the gel column at the same time (t=1680 h), EDAX analysis provide the composition of crystal faces that were growing simultaneously. Each Roozeboom plot corresponds to one of the three characteristic habits: tabular, arrow, and needle-like. As can be seen in Fig. 4a, {001} and {210} faces of the tabular morphology are Ba-rich even for crystals grown from very Sr-rich mother solutions. However, strontium incorporates preferentially on (001) faces than on {210} faces. In the "arrow-like" morphology (Fig. 4b) the situation is similar, i.e. the concentration of Sr is higher on {001} faces than on {210} faces. The characteristic rough {011} surfaces of this morphology have a Sr content similar to that of adjacent {210} faces. Finally, Fig. 4c shows that the

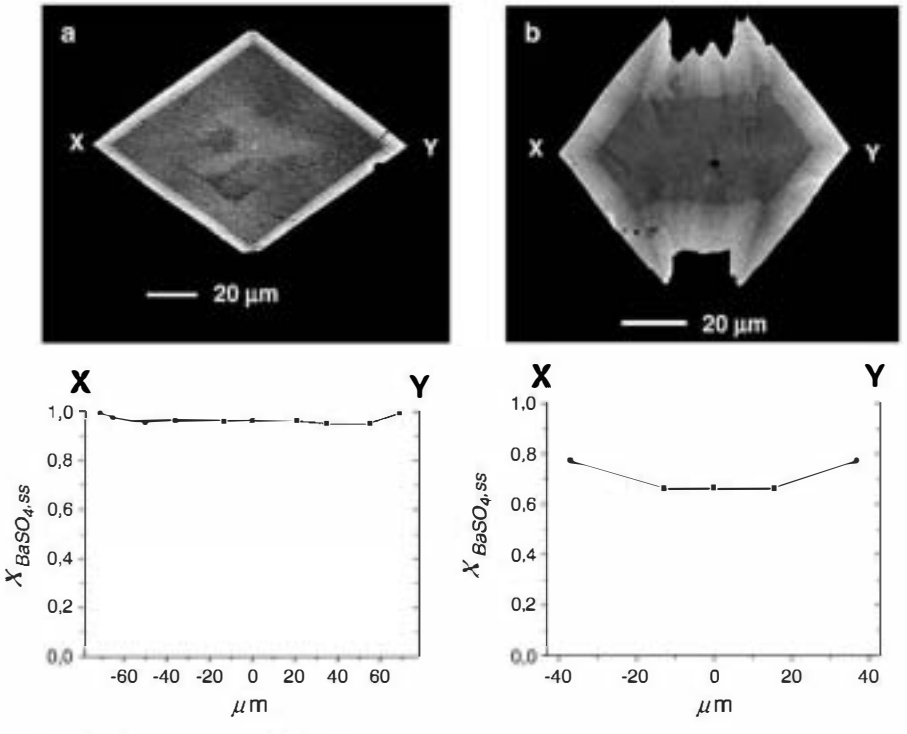

Fig. 5. BSE images of polished $Ba_xSr_{1-x}SO_4$ crystals showing the evolution of internal morphologies (crystals from gel experiments 9 and 8). In these images darker areas correspond to regions with higher Sr contents: (a) tabular crystal. The internal morphology remains constant during the whole growth process. (b) Short arrow-like crystal showing an elongated internal morphology. Note that as growth proceeds {210} form becomes predominant and the characteristic tabular habit of barite is progressively reached. The profiles
each crystal.

needle-like morphologies are very Sr-rich. Here it is important again to note that Roozeboom diagrams in Fig. 4 have been constructed with reference to the initial composition of the mother solution. Therefore, they do not represent the distribution coefficients between the growing crystal face and the evolving surrounding solution.

The relationship between the morphology of the $Ba_xSr_{1-x}SO_4$ crystals and their composition observed along the gel column is also evident in the sections through the crystals. Both BSE images and microprobe analysis of polished sections show progressive compositional zoning of the crystals. For tabular and arrow-like crystal habits microprobe analyses show Ba enrichment from the core to the rim of the crystals. In the case of tabular crystals grown from Ba-rich solutions the enrichment trend is gradual and the $X_{BaSO_4,ss}$ remains high during the whole growth process. Internal morphology of these tabular crystals, recorded as differences in contrast in BSE images, is identical to their external habit (Fig. 5a). Conversely, tabular crystals grown from Sr-rich solutions display stronger compositional gradients from the core to the rim, with $X_{BaSO_4,ss}$ spanning a range as wide as 0.2 (core) to 0.8 (rim). Such strong gradients are accompanied by clear changes in growth morphology. Thus, the central regions of the crystals are relatively Sr-rich and show elongated arrow-like internal habit (Fig. 5b). These internal morphologies can even become "needle-like" when the $X_{BaSO_4,ss}$ is lower than 0.2 (Fig. 6a). However, as the Ba content increases, tabular morphology is progressively reached. The degree of development of the tabular morphology depends on both the $X_{BaSO_4,ss}$ of the core and the length of the growth period. Therefore, crystals which are initially Sr-rich grow for a longer time before reaching a tabular habit than those with Ba-rich cores. Unlike tabular and arrow-like crystals, needle-like crystals are very Sr-rich with a core enriched in Ba and they do not show changes in habit during growth (Fig. 6b).

3.2. AFM observations

In situ AFM experiments were conducted in order to obtain information about the growth kinetics of the $Ba_xSr_{1-x}SO_4$ solid solution at a nanoscale. Changes in morphology described in Section 3.1 are due to changes in the relative growth rates of individual crystal faces

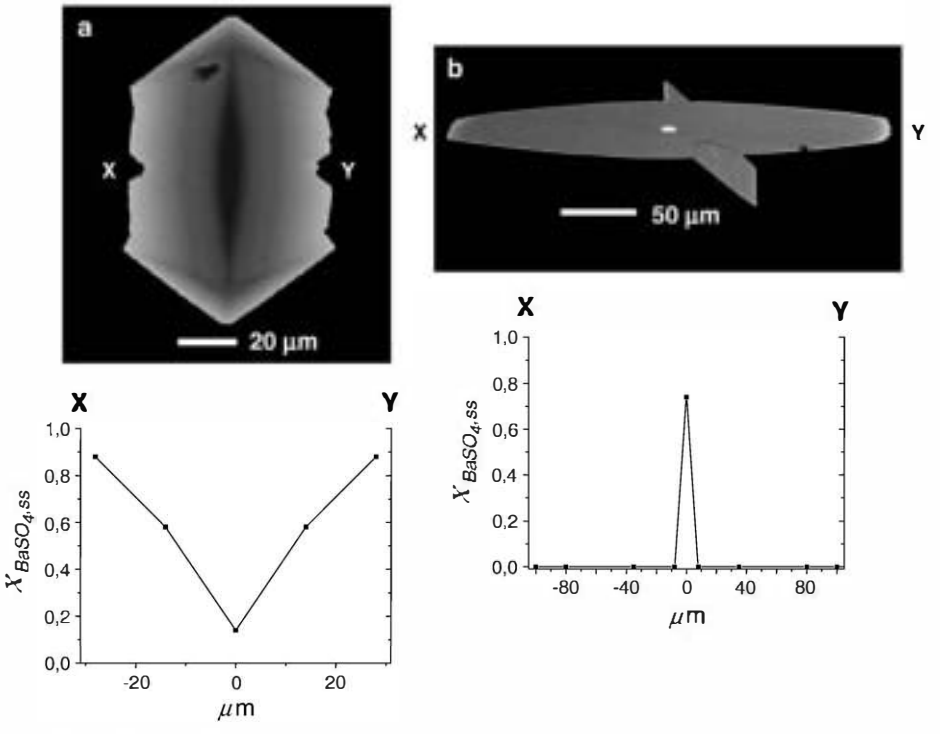

Fig. 6. BSE images of polished $Ba_xSr_{1-x}SO_4$ crystals showing the evolution of internal morphologies (crystals from gel experiments 6 and 4). In these images darker areas correspond to regions with higher Sr contents: (a) long "arrow-like" crystal with a needle-like internal morphology. (b) Needle-like crystal of virtually pure celestite, with a small Ba-rich core. The profiles
crystal.

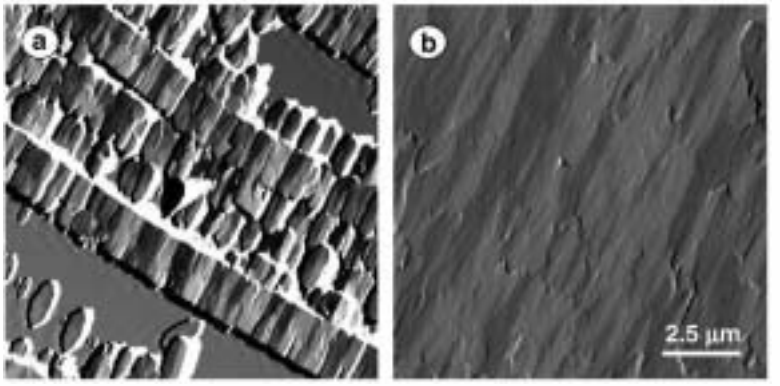

Fig. 7. Two images showing the formation of a homogeneous epitaxial layer of celestite on a barite (001) surface. The time elapsed between both images was about 10 min. The composition of the growth solution was: $a(Sr^{2+})=2.5\times10^{-3}$, $a(SO_4^{2-})=2.4\times10^{-3}$. The supersaturation of the solution with respect to celestite was $\beta_{celestite}=26.9$ (AFM experiment number 5). Images were taken in constant force mode while displaying the cantilever deflection

that, in principle, can be measured at a molecular scale. To evaluate this, we have studied the growth kinetics of pure $SrSO_4$ on barite (001) surfaces (for a detailed study of the kinetics of epitaxial growth of celestite on barite (001) surface see Sánchez-Pastor et al. (2005)). There are several reasons for this choice: (i) the growth behaviour at a nanoscale of the (001) face on barite is relatively well known (Pina et al., 1998a,b; Bosbach et al., 1998) and, therefore, our observations can be compared to this reference; (ii) the (001) face is the one most affected by changes in composition during growth since it is dominant on our Ba-rich crystals, but it is absent in our Sr-rich crystals); and (iii) it is possible to measure growth rates on the (001) surface along directions which are perpendicular to the barite–celestite most important forms: (001), (100), (210) and (011).

When a freshly cleaved (001) face of barite is placed in contact with flowing $SrSO_4$ solutions at a supersaturation with respect to celestite (calculated using Eq. (1)) higher than around 10, the formation of two-dimensional islands is observed after a few seconds. These celestite islands show a habit defined by {001}, {210} and {100} forms. The distribution of islands on the (001) barite surface is not random as they preferentially nucleate along the cleavage steps. The lateral growth of the islands leads to their rapid coalescence, defining continuous bands along former cleavage steps and, after a few minutes, the whole substrate surface is covered by a celestite homogeneous layer (see Fig. 7).

Fig. 8 shows an AFM image indicating the crystallographic planes for which celestite islands growth rates were measured for seven different supersaturations with

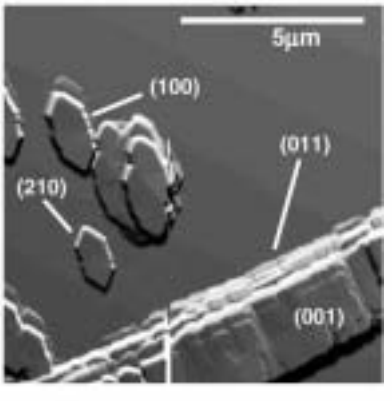

Fig. 8. Typical AFM image of celestite growing on a barite (001) surface. The crystal planes for which growth rates have been measured are indicated in the image. The image was taken in constant force mode while displaying the cantilever deflection

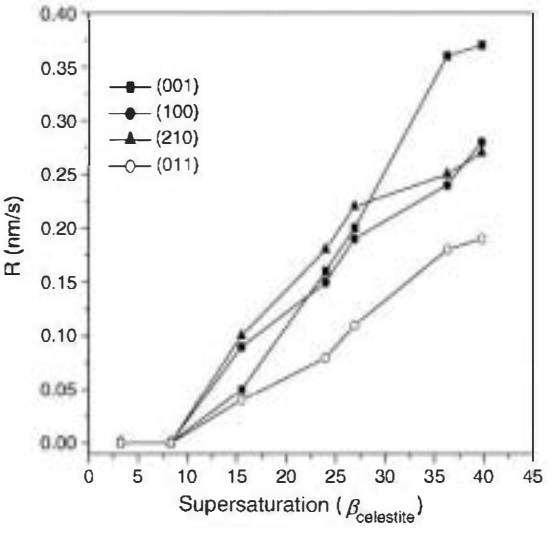

Fig. 9. Curves showing the variation of different faces growth rate with supersaturation. Growth rates have been determined from sequences of AFM images.

respect to $SrSO_4$. Fig. 9 shows a plot of growth rates on the different faces against supersaturation. As can be seen, no growth is observed at supersaturation values lower than about 10. As supersaturation increases, growth rates on the different faces increase differently. While (100) and (210) faces have similar to each other growth rates in the whole range of supersaturations studied, (001) and (011) faces grow at almost the same rate at supersaturations below 15. Beyond this supersaturation value their relative growth rates differ increasingly as supersaturation increases. At supersaturation around 40, (011) is the face with the smallest growth rate, while (001) shows the fastest growth.

4. Discussion

As our results show, the crystallization behaviour of $Ba_xSr_{1-x}SO_4$ solid solution is very sensitive to changes in aqueous solution composition. The compositional feature common to crystals formed during the first and second nucleation events is that their cores are richer in Sr than predicted from equilibrium thermodynamics considerations. This is reflected by the less pronounced curvature of the Roozeboom line constructed using crystals cores compositions compared to equilibrium Roozeboom line (Fig. 3). According to the equilibrium curve, the first crystal growing should be almost pure barite in all the experiments, even for a $X_{[Ba^{2+}],aq}$ of 0.1 ($Ba_{0.999}Sr_{0.001}SO_4$ for $X_{[Ba^{2+}],aq}=0.9$ and $Ba_{0.996}Sr_{0.004}SO_4$ for $X_{[Ba^{2+}],aq}=0.1$). However, crystals cores always contain a certain amount of Sr, which increases as $X_{[Ba^{2+}],aq}$ in the mother solution decreases ($Ba_{0.95}Sr_{0.05}SO_4$ for $X_{[Ba^{2+}],aq}=0.9$ and $Ba_{0.35}Sr_{0.65}SO_4$ for $X_{[Ba^{2+}],aq}=0.1$). This is a direct consequence of the high supersaturation at nucleation time and during the early stages of growth process. As Prieto et al. (1997) demonstrated, in solid solution–aqueous solution systems, high supersaturation conditions favour the crystallization of more soluble solid solution compositions. To understand crystallization kinetics in diffusing–reacting systems as the one under consideration, it is essential to introduce the "threshold supersaturation" concept. This concept is equivalent to critical supersaturation, but applies to non-homogeneous systems, where composition gradients exist and supersaturation evolves with time (Prieto et al., 1990). Prieto et al. (1993) determined under conditions similar to this study that the "threshold supersaturation" value is about two orders of magnitude higher for the nucleation of the Ba-rich end-member (barite) than for the nucleation of the Sr-rich end-member (celestite). This fact results from the very high difference between the solubility products of these end-members (log K_{sp}(barite)=−9.98; log K_{sp}(celestite)=−6.63). In such a system, a higher incorporation of Sr in the solids is kinetically favoured with respect to that predicted by thermodynamics. The high supersaturation under which nucleation occurs in this type of systems corresponds to a large departure from equilibrium and solids grow with compositions closer to those of aqueous solutions. However, as the degree of supersaturation decreases, system approaches equilibrium. This must lead to an increase of the curvature of the Roozeboom lines, i.e. crystals become Ba-richer as growth progresses. This conceptual model is in agreement with our experimental data. Thus, Roozeboom lines constructed from composition data measured on crystals surfaces show higher curvatures than those constructed from data corresponding to crystals cores (see Fig. 3).

On the other hand, changes in crystal chemistry correlate to evident morphological changes, particularly the inhibition of the {001} pinacoid and the increasing importance of the {011} rhombic prism in Sr-rich crystals. As has been mentioned in Section 3.1, Sr incorporates differentially on non-equivalent faces. Plots in Fig. 4a,b show that all forms present in $Ba_xSr_{1-x}SO_4$ crystals show Sr distribution coefficients that exceed equilibrium values. Moreover, the difference is greatest for (001) surfaces. {210} and {011} show very similar experimental Sr distribution coefficients. Therefore, the relationship between morphological and compositional changes in $Ba_xSr_{1-x}SO_4$ crystals can be interpreted as a result of the differences in growth rates between different crystallographic forms, arising from surface-specific differences in Sr incorporation. This is in agreement with the results of our AFM experiments.

The periodic bond chain (PBC) theory was applied to barite type structure by Hartman and Perdok (1955) shortly after its development. According to these authors, the following faces can be considered as having an F-character: {002}, {210}, {101}, {211}, {020} and {200}. As has been mentioned above, the habit of $Ba_xSr_{1-x}SO_4$ crystals grown in silica gel is controlled by {001}, {210} and {100} forms when the crystal composition is close to pure barite. All the forms present in the habit are F-forms and the resulting growth morphology is very close to the theoretical habit calculated by Hartman and Perdok (1955). However, when the composition of $Ba_xSr_{1-x}SO_4$ crystals approaches to the Sr-rich end-member, the habit of the crystals is mainly controlled by {011} forms, with {210} as a less important form and {100} as a very minor form. In Sr-rich crystals {001} is absent and its

morphological importance increases with the increase of Ba-content in $Ba_xSr_{1-x}SO_4$ crystals. The character of the {011} form is controversial. The studies of the theoretical morphology of barite type crystals carried out by Dowty (1976) and Tassoni et al. (1978) basically agreed with the results of Hartman and Perdok (1955). However, these authors also included {011} among their F forms, whereas it had been considered a K form by Hartman and Perdok (1955). The character of {011} form has been lately reconsidered by Hartman and Strom (1989). According to these authors {011} is an F form for which 33 different slices can be defined. A number of {011} configurations have similar attachment energies and they can coexist on {011} surfaces during growth. This results in a rough surface and, therefore, (011) face behaves as a K face. However, as most of the slices that could be defined to explain the growth of this form have either cation or sulphate ions in their outermost layer, it can be stabilized by preferential impurity adsorption. According to our experimental results, when the incorporation of Sr and Ba into the crystal has a similar magnitude, (011) face shows a high surface roughness, suggesting that it behaves as a K form. However, a higher incorporation of Sr may stabilize those surface configurations with lower energies. It could even occur that a single configuration prevails. This particular aspect would need to be confirmed by further direct nanoscale observations. Under this scenario, as the crystal becomes Sr-richer, the (011) form increases its F character. It is worth noting that, as Hartman and Strom (1989) pointed out, {011} is the prevailing form in most natural celestite crystals. This growth behaviour is consistent with our SEM observations, which have shown that Sr enrichment in crystals correlates to more important and smoother {011} faces.

Obviously, morphological changes in $Ba_xSr_{1-x}SO_4$ crystals as their Sr content increases are a direct consequence of changes in the relative growth rate of the main crystallographic forms. The largest variations in relative growth rates as a function of supersaturation are displayed by {001} and {011} forms. By contrast, relative growth rates of {210} and {100} remain constant for the supersaturation range considered. In order to visualize the effect of these relative growth rates on morphology, three crystal habits have been drawn from the experimental data corresponding to three supersaturation values: $\beta_{celestite}=15.5$, $\beta_{celestite}=26.9$ and $\beta_{celestite}=39.8$ (Fig. 10). As a result of the rapid increase of (001) growth rate with supersaturation, this face is absent in the growth morphology corresponding to high supersaturations. On the other hand, the relative importance of (011) faces increases with supersaturation with respect to celestite. The changes in crystal habit deduced from AFM measurements are in agreement with the changes in both external and internal habits of the $Ba_xSr_{1-x}SO_4$ crystals observed in our gel experiments. Furthermore, these changes in crystal habits are also consistent with typical habits reported for natural celestite, barites and Sr-bearing barites (Kostov and Kostov, 1999 and references therein).

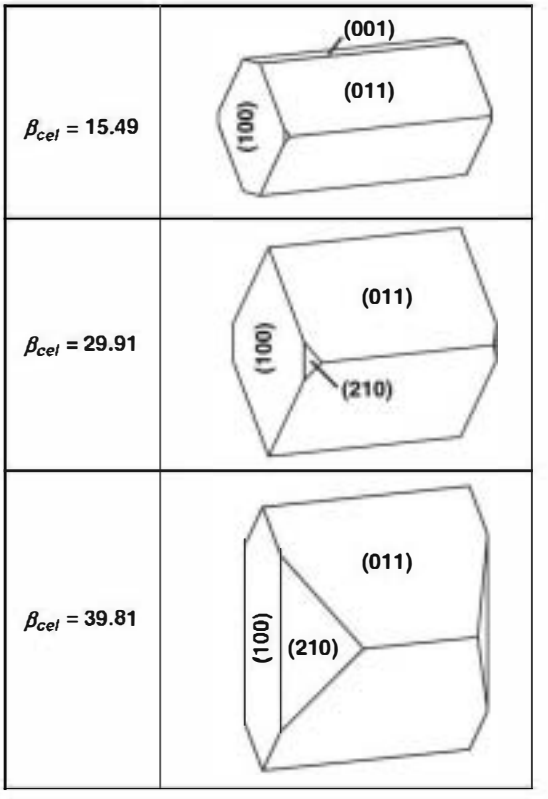

Fig. 10. $Ba_xSr_{1-x}SO_4$ growth morphology at three supersaturations with respect to celestite. The growth rates for the different faces were obtained from AFM experiments.

5. Conclusion

This work has shown that the morphology of $Ba_xSr_{1-x}SO_4$ crystals grown in a diffusing–reacting system strongly depends on the solid solution composition. This type of systems, where substantial supersaturation and compositional gradients develop, makes it possible to observe a correlation between composition and crystal habit as they change both in space and time. Thus, a crystal habit sequence from tabular to needle-like crystals is observed along the diffusion column as the $X_{[Ba^{2+}],aq}$ ratio in the medium decreases. On the other hand, internal zoning in individual crystals

also records the relationship between composition and crystal habit. As growth proceeds, individual crystals become Ba-richer and their habit evolves from needle-like to tabular, a consequence of an increase in the morphological importance of {001} form and a progressive decrease of {011}, which is always absent from crystals close to pure barite. Therefore, $X_{[Ba^{2+}],aq}$ in the growth medium exerts a strong control on the growth rate of the different crystallographic faces. High concentrations of Sr stabilize the {011} form. This, together with the increase of the growth rate on (001), leads to the development of habits elongated along [001], in which {011} is the main form. AFM experiments confirm the effect of Sr on face-specific growth rates. Measurements at a molecular scale of the growth of celestite on a barite (001) face show that, as the supersaturation with respect to celestite increases, the difference between the growth rates of {001} and {011} become more important.

The results presented in this study show the strong effect of compositional variability on the $Ba_xSr_{1-x}SO_4$ crystal morphology. The presence of different ions and/or growth inhibitors in natural environments could explain the wide range of habits of hydrothermal and authigenic barites. In the future, we may gain a better understanding of the factors controlling barite–celestite crystallization by comparing natural morphologies with those obtained under well defined experimental conditions.

Acknowledgements

Authors thank Manuel Prieto for critical reading of the manuscript. The barite sample was kindly provided by Begoña Sánchez and Javier García-Guinea (Museo Nacional de Ciencias Naturales, Spain). AFM experiments were conducted at the Institut für Mineralogy Münster (Germany). Two anonymous reviewers are thanked for their critical comments, which significantly improved the paper. C.M. Pina and N. Sánchez-Pastor acknowledge Spanish Ministry of Education and Science for financial support (Ramón y Cajal contract and FPI grant, respectively). This work has been financially supported by the Spanish Ministry of Education and Science (Project BTE2002-00325). [LW]

References

Bernstein, R.E., Byrne, R.H., 2004. Acantharians and marine barite. Mar. Chem. 86, 45–50.

Bernstein, R.E., Byrne, R.H., Betzer, P.R., Greco, A.M., 1992. Morphologies and transformations of celestite in seawater: the role of acantharians in strontium and barium geochemistry. Geochim. Cosmochim. Acta 56, 3273–3279.

Bishop, J.K.B., 1988. The barite–opal–organic carbon association in oceanic particulate matter. Science 332, 341–343.

Blount, C.W., 1977. Barite solubilities and thermodynamics quantities up to 300 °C and 1400 bars. Am. Mineral. 62, 942–957.

Bosbach, D., Hall, C., Putnis, A., 1998. Mineral precipitation and dissolution in aqueous solution: in-situ microscopic observations on barite (001) with atomic force microscopy. Chem. Geol. 151 (1–4), 143–160.

Chow, T.J., Goldberg, E.D., 1960. On the marine geochemistry of barium. Geochim. Cosmochim. Acta 20, 192–198.

Claypool, G.E., Holser, W.T., Kaplan, I.R., Sakai, H., Zak, I., 1980. The age curves of sulfur and oxygen isotopes in marine sulfate and their mutual interpretation. Chem. Geol. 28 (3–4), 199–260.

Dehairs, F., Chesselet, R., Jedwab, J., 1980. Discrete suspended particles of barite and the barium cycle in the open ocean. Earth Planet. Sci. Lett. 49, 528–550.

Dowty, E., 1976. structure and crystal-growth. 1. Influence structure on morphology. Am. Mineral. 61 (5–6), 448–459.

Feely, R.A., 1987. Distribution of chemical tracers in the eastern equatorial Pacific
ern Oscillation event. J. Geophys. Res. 92, 11343–11363.

Ganeshram, R.J., Francois, R., Commeau, J., Brown-Leger, S.L., 2003. An experimental investigation of barite formation in seawater. Geochim. Cosmochim. Acta 67, 2599–2605.

Hartman, P., Perdok, W.G., 1955. On the relations between structure and morphology of crystals. Acta Crystallogr. 8 (9), 525–529.

Hartman, P., Strom, C.S., 1989. Structural morphology of crystals with the barite ($BaSO_4$) structure: a revision and extension. J. Cryst. Growth 97, 502–512.

Henisch, H.K., 1988. "Growth waves" in periodic precipitation. J. Cryst. Growth 87, 571–572.

Kastner, M., 1999. Oceanic minerals: their origin, nature of their environment, and significance.
3380–3387.

Kostov, I., Kostov, R.I., 1999. Crystal habits of minerals. Co-published by Prof. Marin Drinov Academic Publishing House and Pensoft Publishers Sofi

Lloyd, G.E., 1987. Atomic number and crystallographic contrast images with the SEM: a review of back-scattered electron techniques. Min. Mag. 51, 3–19.

Parkhurst, D.L., Appelo, C.A.J. 2000. User's guide to PHREEQC (version 2). A computer program for speciation, batch-reaction, one-dimensional transport, and inverse geochemical calculations. USGS Water-Resour. Invest., 312.

Paytan, A., Kastner, M., Martin, E.E., Macdougall, J.D., Herbert, T., 1993. Marine barite as a monitor of seawater strontium isotope composition. Nature 366, 445–449.

Paytan, A., Mearon, S., Cobb, K., Kastner, M., 2002. Origin of marine barite deposites: Sr and isotope characterization. Geology 30, 747–750.

Pina, C.M., Becker, U., Risthaus, P., Bosbach, D., Putnis, A., 1998a. Molecular-scale mechanisms of crystal growth in barite. Nature 395 (6701), 483–486.

Pina, C.M., Bosbach, D., Prieto, M., Putnis, A., 1998b. Microtopography of the barite (001) face during growth: AFM observations and PBC theory. J. Cryst. Growth 187, 119–125.

Prieto, M., Putnis, A., Fernández-Díaz, L., 1990. Factors controlling the kinetics of crystallization: supersaturation evolution in a porous medium. Application to barite crystallization. Geol. Mag. 127, 485–495.

Prieto, M., Fernández-Díaz, L., López-Andrés, S., 1991. Spatial and evolutionary aspects of nucleation in diffusing–reacting systems. J. Cryst. Growth 108, 770–778.

Prieto, M., Putnis, A., Fernández-Díaz, L., 1993. Crystallization of solid solutions from aqueous solutions in a porous medium: zoning in (Ba, Sr)SO_4. Geol. Mag. 130, 289–299.

Prieto, M., Fernández-Díaz, L., López-Andrés, S., 1994. Metastability in diffusing–reacting systems. J. Cryst. Growth 108, 770–778.

Prieto, M., Fernández-González, A., Fernández-Díaz, L., 1997. Nucleation, growth, and zoning phenomena in crystallizing (Ba,Sr)CO_3, Ba(SO_4,CrO_4), (Ba,Sr)SO_4, and (Cd,Ca)CO_3 solid solutions from aqueous solutions. Geochim. Cosmochim. Acta 61, 3383–3397.

Putnis, A., Fernández-Diaz, L., Prieto, M., 1992. Experimentally produced oscillatory zoning in the (BaSr)SO_4 solid solution. Nature 358, 743–745.

Reardon, E.J., Armstrong, D.K., 1987. Celestite ($SrSO_4$(s)) solubility in water, sea water and NaCl solution. Geochim. Cosmochim. Acta 51, 63–72.

Rushdi, A.I., McManus, J., Collier, R.W., 2000. Marine barite and celestite saturation in seawater. Mar. Chem. 69, 19–31.

Sánchez-Pastor, N., Pina, C.M., Astilleros, J.M., Fernández-Díaz, L., 2005. Epitaxial growth of celestite on barite (001) face observed at a nanoscale. Surf. Sci. 581, 225–235.

Tassoni, D., Riquet, J.P., Durand, F., 1978. Programmed research on periodic bond chains. Acta Crystallogr., A 34, 55–60.